Geophys. J. Int. (2009) **178,** 1238–1245 doi: 10.1111/j.1365-246X.2009.04250.x

Permanent Scatterer investigation of land subsidence in Greater Cairo, Egypt

M. H. Aly,[1] H. A. Zebker,[2] J. R. Giardino[3] and A. G. Klein[4]

[1]*Department of Earth Sciences, University of California-Riverside, Riverside,* CA 92521-0423, *USA. E-mail: drmaly@ucr.edu*
[2]*Department of Geophysics, Stanford University, Stanford,* CA 94305-2215, *USA*
[3]*Department of Geology & Geophysics, Texas A&M University, College Station,* TX 77843-1113, *USA*
[4]*Department of Geography, Texas A&M University, College Station,* TX 77843-3174, *USA*

Accepted 2009 May 11. Received 2009 April 19; in original form 2008 September 12

SUMMARY

Land subsidence is a major geomorphic problem commonly associated with densely populated areas, such as the Greater Cairo area. Prior to this study, rates and patterns of land subsidence in Greater Cairo were not known. The Permanent Scatterer interferometric approach has been applied in this study to detect and measure the magnitude and the spatial and temporal variations of subsidence in Greater Cairo. Thirty-four Interferometric Synthetic Aperture Radar (InSAR) images acquired by the European Radar Satellites (ERS-1 and ERS-2) during 1993–2000 have been used in this investigation. The main contributing factors to the rate of land subsidence in Greater Cairo include natural sediment compaction, tectonic activity and groundwater pumping. However, the measured rate of land subsidence is found significantly impacted by anthropogenic factors rather than natural factors. The average measured rate of subsidence is approximately 7 mm yr^{-1} during the period of observation, and the spatial and temporal patterns of land subsidence are demonstrated by a time-series of surface deformation maps. InSAR results show differential surface displacements along the major surface and subsurface faults and indicate pumping-induced subsidence, which is characterized by bowl shapes, in districts of high population density. The detected pattern of land subsidence in Greater Cairo implies a considerable contribution from the subway network as well. The results from this interferometric investigation can be used to help mitigate the environmental impacts and potential consequences of land subsidence in the region.

Key words: Time series analysis; Image processing; Satellite geodesy; Radar interferometry; Africa.

1 INTRODUCTION

Cairo, the capital of Egypt, is a large city located along the banks and islands of the Nile River at the apex of the Nile Delta where the Nile River splits into two branches (Fig. 1). Cairo has an extensive, prosperous history and is considered one of the most important historical cities in the world. With approximately 20 million inhabitants, Cairo is also one of the most densely populated cities on Earth. Greater Cairo encompasses three adjacent administrative governorates and its region has been continuously inhabited during the past 6000 yr. Greater Cairo is expanding rapidly, which has created numerous environmental problems.

Land subsidence is a major geomorphic problem in the Nile Delta (Fig. 1) of Egypt. The main contributing factors to the rate of land subsidence in the delta include natural sediment compaction, tectonic activity, groundwater pumping and hydrocarbon extraction. Stanley (1988, 1990) estimated the rates of land subsidence near the Mediterranean coast to be between 1.00 and 2.50 mm yr^{-1} in the west and 5.00 mm yr^{-1} in the east. These rates were estimated based on radiocarbon dating of the Holocene deltaic sediments. Zaghloul *et al.* (1977), Said (1981), Stanley (1988, 1990) and Stanley & Warne (1993) attributed the rapid rate of subsidence in the eastern side of the delta to stratigraphic and tectonic factors. Warne & Stanley (1993) reassessed the estimated rates by Stanley (1988, 1990) and concluded that they are minimum rates because sediment reworking can cause radiocarbon dated cores to be older than the burial age. However, subsidence rates estimated based on this geological process are assumed to have uniform extensions across the delta, yielding only spatial and temporal averages; therefore, there is no unique rate of subsidence that can be assigned to a particular location.

Groundwater has been a major source of municipal and domestic water supply in Greater Cairo during the past century. The dramatic increase in population density during the past few decades has led to a significant increase in the rate of groundwater pumping. This, in turn, has resulted in a significant acceleration of the rate of urban subsidence. Declining groundwater in the aquifer system has impacted also the rate of long-term subsidence as a result of

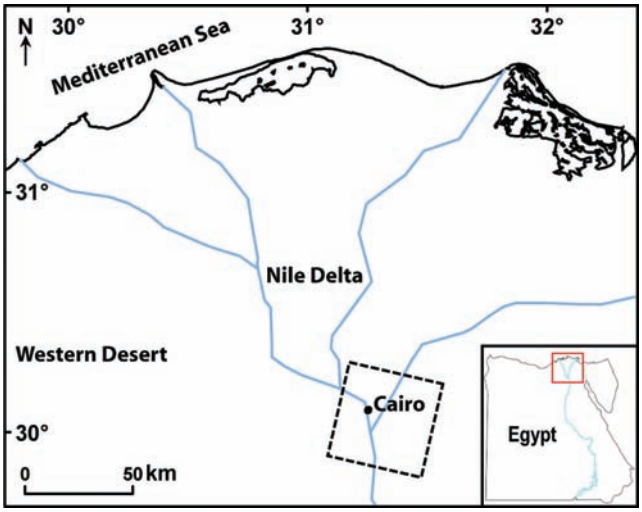

Figure 1. Location map of Greater Cairo. The dashed black lines indicate the ERS subscene footprint (Track: 436, Frame: 2997) used in the PS analysis.

compaction of the aquifer system that consists mainly of unconsolidated sediments composed of significant fractions of silts, clays and sands.

Potential consequences of land subsidence in Greater Cairo include, but are not limited to, reduction of the aquifer system storage and damage to the utility infrastructures, wells, railroads, highways, bridges and buildings. Therefore, there is an increasing demand for regular monitoring and accurate measuring of the rates and patterns of land subsidence to support the integrated sustainable development of Greater Cairo.

Traditional levelling surveys and Global Positioning System (GPS) measurements are widely used in measuring land subsidence, but these are point-measurement tools and, thus, provide spatially limited views of the ongoing deformation. In contrast, Synthetic Aperture Radar interferometry (InSAR) provides subtle deformation measurements at a significantly improved resolution with millimetre-level accuracy over large areas. InSAR has been applied successfully in measuring land subsidence by many researchers; for example, Fielding *et al.* (1998), Galloway *et al.* (1998), Amelung *et al.* (1999), Fruneau *et al.* (1999), Strozzi & Wegmüler (1999), Strozzi *et al.* (1999a,b), Ferretti *et al.* (2000), Bawden *et al.* (2001), Hoffmann *et al.* (2001), Buckley *et al.* (2003), Casu *et al.* (2005), Dixon *et al.* (2006), Galloway & Hoffmann (2006) and Motagh *et al.* (2008).

Prior to our study, the actual rates of land subsidence and its spatial and temporal variations in Greater Cairo were not known. Stabel & Fischer (2001) attempted to measure urban subsidence in Cairo using satellite InSAR, but the study was unsuccessful because they could not construct or find a suitable Digital Elevation Model (DEM) to correct the interferometric phase for topography. In our study, we were able to use Permanent Scatterer (PS) interferometry to detect land subsidence and its patterns in Greater Cairo. The study area is characterized by a very dense settlement structure and bare rocks with sparse vegetation, which provided an appropriate environment for the PS analysis.

2 PERMANENT SCATTERER ANALYSIS

The PS interferometric approach was first introduced by Ferretti *et al.* (2000). Since then, it has been applied successfully in many surface deformation studies, such as estimating the rate of nonlinear subsidence (Ferretti *et al.* 2000; Bell *et al.* 2008), monitoring landslides and tectonic motions (Colesanti *et al.* 2003), detecting mining related ground instabilities (Colesanti *et al.* 2005) and measuring strain accumulation along fault zones (Motagh *et al.* 2007). Recently, several approaches with further improvements have been developed; for example, Dehls *et al.* (2002), Adam *et al.* (2003), Crosetto *et al.* (2003) and Hooper *et al.* (2004). In fact, the PS analysis can be conducted in various ways according to the technical problems in the InSAR data set being processed. In this study, we employed a similar approach to the one developed by Ferretti *et al.* (2000), with several deviations in the processing procedure, as described in the following subsections.

2.1 Image creation and registration

In PS interferometry, all InSAR pairs, regardless of their perpendicular and temporal baselines, can be involved in the analysis. Therefore, 34 descending ERS-1/2 scenes (Track: 436, Frame: 2997), spanning 8 yr from 1993 to 2000 with varying normal baselines (Table 1), were used in the PS analysis. The raw ERS scenes were processed to a Doppler Centroid independent of range sample to generate Single Look Complex (SLC) images. To avoid the densely vegetated areas of no interferometric coherence, a small subset (about 33 km $\times$ 28 km) of the ERS scenes covering the urban areas in Greater Cairo (Fig. 1) was used for conducting the PS analysis.

As ERS images are acquired from slightly different angles at different times, offsets do occur. Consequently, all SLC images have to be resampled and registered to a reference image before conducting the PS analysis. This is done by determining the offsets between corresponding pixels in two SLCs (the reference and the resampled images) and by calculating and applying a rotation and skew matrix that registers the resampled SLC image to the reference. The reference image has to be selected carefully as all the PS measurements will be relative to the selected reference. To select a unique reference image, ERS pairs of limited atmospheric artefacts were determined using the approach of pairwise comparison of interferograms developed by Massonnet & Feigl (1995). The approach provides an assessment of the initial interferograms without statistical analysis of the high-level products, and it does not require ancillary data spatially and temporally coincident with the SAR acquisitions.

Interferograms with high coherence were generated from ERS tandem pairs, using ERS images acquired with 24-hr apart from each other (Table 1). The tandem interferograms were then compared using the pairwise comparison approach to assess the degree to which atmospheric artefacts are present in each pair. The comparison revealed that interferograms generated from summer acquisitions during August and September were impacted significantly by large amplitude, high frequency atmospheric artefacts as a result of the substantial heating in summer months. Interferograms generated from winter acquisitions were found less affected by atmospheric artefacts. Based on these comparisons, the ERS-2 scene acquired on 1996 January 11 has been selected as the reference. It has low atmospheric distortions and minimizes both the perpendicular and the temporal baselines in the data set, as well as, has a Doppler Centroid near the average of the other SAR acquisitions.

The registration accuracy assessment revealed that all SLC images were precisely registered to the selected reference, and the standard deviations of the individual range and azimuth offset estimates from the regression fit were less than 0.10 pixel. All ERS scenes were oversampled by a factor of two to avoid aliasing errors in the registration process using amplitude values. The initial pixel

Table 1. ERS data set used in the PS analysis.

Number	Date (dd/mm/yyyy)	Perpendicular baseline, $B_\perp$ (m)	Temporal baseline, B_T (d)	ERS
1	12/04/1993	617.0048	–1004	1
2	17/05/1993	−77.6699	−969	1
3	26/07/1993	249.5015	−899	1
4	04/10/1993	−50.3564	−829	1
5	14/06/1995	−87.0998	−211	1
6	23/08/1995	−22.3913	−141	1
7	24/08/1995	−122.5054	−140	2
8	27/09/1995	150.3387	−106	1
9	28/09/1995	567.0938	−105	2
10	06/12/1995	169.0418	−36	1
11	10/01/1996	125.4489	−1	1
12	11/01/1996	0.0000	0	2
13	14/02/1996	655.5337	34	1
14	15/02/1996	663.9315	35	2
15	24/04/1996	872.8420	104	1
16	29/05/1996	−354.5767	139	1
17	30/05/1996	−463.0765	140	2
18	15/05/1997	35.2625	490	2
19	09/07/1998	−438.0561	910	2
20	17/09/1998	−770.1791	980	2
21	31/12/1998	−783.9076	1085	2
22	11/03/1999	−64.2046	1155	2
23	15/04/1999	749.9412	1190	2
24	20/05/1999	−187.5423	1225	2
25	07/10/1999	−302.3993	1365	2
26	16/12/1999	552.6185	1435	2
27	20/01/2000	−126.4835	1470	2
28	23/02/2000	−897.5716	1504	1
29	24/02/2000	−728.0547	1505	2
30	30/03/2000	−300.7856	1540	2
31	04/05/2000	−224.0248	1575	2
32	08/06/2000	−140.1180	1610	2
33	26/10/2000	−310.1321	1750	2
34	30/11/2000	−234.8034	1785	2

dimensions of ERS images are approximately 4 m × 20 m in azimuth and range directions, respectively. They were multilooked, 10 looks in the azimuth direction and two looks in the range direction, to reduce the speckle and produce pixels with approximately 40 m dimensions in both azimuth and range directions.

The average amplitude image of 34 ERS subscenes is shown in Fig. 2, which shows the mean intensities of the radar backscatter and surface features in the study region. The Nile River and major roads appear in dark grey tones. The Cairo International Airport, in the northeastern part of the average amplitude image, appears also in dark grey tones. Built up areas in Greater Cairo have a bright radar response, whereas cultivated areas appear in light grey tones.

2.2 Selection of the Permanent Scatterers

The amplitude dispersion index (D_a), which is the ratio of the standard deviation of the amplitude (σ_a) to its mean (μ_a), was applied to identify the PSs in Greater Cairo. The amplitude dispersion index is a measure of phase stability and is practically proved to be powerful in detecting PSs over bare rocks and man-made structures. The lower the amplitude dispersion index, the higher the phase stability.

$$D_a = \sigma_a/\mu_a. \tag{1}$$

Before statistically analysing the amplitude values, all amplitude images were calibrated radiometrically using calculated calibration factors from the processed data set so that all images were comparable. The amplitude images were averaged and the mean of the stack and the standard deviation from the mean were then calculated. Consequently, the average calibration factor was calculated for each image in the stack using the ratio of the amplitude of each image to the mean amplitude of the entire stack. All points of low amplitude dispersion, $D_a < 0.25$, were then selected as PSs. An average density of 157 PS km^{-2} was identified, which was sufficient for aliasing the spatial variations of land subsidence in Greater Cairo.

2.3 Interferogram generation and phase correction

SLC values were extracted for the identified PSs, and the complex interferograms were calculated from these values by multiplying the reference image with the complex conjugate of the resampled image, yielding the phase difference between the two SAR acquisitions for each PS. The complex interferometric phase (ϕ_{comp}) at pixel (p) in interferogram (i) is nominally a summation of six phase components, which are

$$\phi_{\text{comp},p,i} = \phi_{\text{def},p,i} + \phi_{\text{topo},p,i} + \phi_{\text{orb},p,i} + \phi_{\text{flat},p,i} + \phi_{\text{atm},p,i} + \phi_{\text{noise},p,i}, \tag{2}$$

where ϕ_{def} is the deformation phase, ϕ_{topo} is the topographic phase, ϕ_{orb} is the orbital phase, ϕ_{flat} is the flat Earth phase, ϕ_{atm} is the atmospheric phase and ϕ_{noise} is the phase noise.

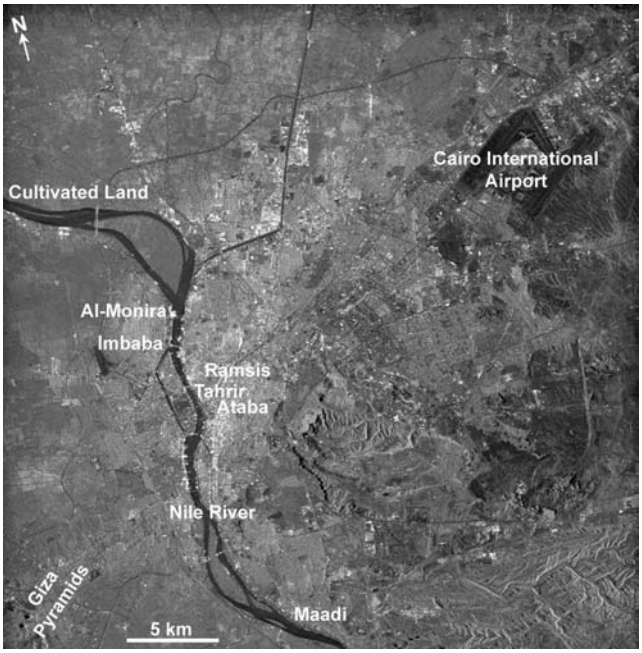

Figure 2. Average amplitude image of 34 ERS subscenes spanning 1993–2000. The Nile River and major roads, as well as Cairo International Airport appear in dark grey tones. Urban areas appear in a bright radar response, and cultivated areas appear in light grey tones.

The basic strategy in PS interferometry is to estimate and separate the aforementioned phase components from the deformation phase for each PS. The topographic phase was removed using a DEM of a 3-arcsec spatial resolution created from the digital elevation data provided by the Shuttle Radar Topography Mission (SRTM). The topographically corrected interferograms were then filtered using a non-linear adaptive filter developed by Goldstein & Werner (1998) to reduce the amount of phase noise, which is always present in SAR images, and the DEOS precise state vectors (Scharroo & Visser 1998) were used to compensate for orbital inaccuracies.

2.4 Phase unwrapping and error analysis

Both spatial and temporal phase unwrapping were conducted on the topographically corrected interferograms for the selected PSs. The interferograms were first spatially unwrapped using the Minimum Cost-network Flow (MCF) algorithm developed by Costantini (1998), and the spatially unwrapped values of PSs were integrated in time to produce the time series of unwrapped phase for each selected PS.

Visual inspection of the topographically corrected interferograms provided a first-order approximation of phase errors, and temporal and spatial consistencies of features were considered for discriminating deformation features. Persistent phase signals are most likely related to real deformation, as they usually occur at the same location in several interferograms over considerable time spans. In contrast, atmospheric artefacts because of their dynamic nature are not expected to occur exactly at the same location in a time series of interferograms (Zebker *et al.* 1997). Therefore, all patterns observed in several interferograms at the same locations were considered true deformation, and sparse features lacking temporal and spatial consistency were assumed to be atmospheric artefacts rather than real deformation.

To remove the phase due to atmospheric variations, the residual phases were spatially filtered, and the outputs were subject to temporal filtering in order to investigate phase trends in the time series. Subsequently, phase signals that lack spatial and temporal consistency were subtracted from the interferometric phase of the selected PSs. Furthermore, phase signals in the topographically corrected interferograms of very short time spans (Table 1) were assumed to be topographic residuals and/or tropospheric effects and were eliminated, as no measureable deformation is expected to occur in Greater Cairo within a few days.

Phase signals may be affected also by tropospheric variations as a function of altitude. In fact, tropospheric variations can cause errors similar to the topographic residual (Delacourt *et al.* 1998). However, topography-induced effects are not expected in Greater Cairo because the area is relatively flat. However, the soil moisture content in the study region is a major concern, especially in cultivated areas because of the systematic irrigation of crops. Therefore, we limited the PSs selection to the built-up areas in order to avoid the effects of soil moisture content.

The estimation process of phase components was undertaken iteratively to precisely eliminate the residual topographic phase, the atmospheric phase, the phase noise and the flat Earth phase, as well as the phase related to inaccuracies in calculations of the satellite orbits from the interferometric phase, leaving only the phase change related to the surface movements. Ultimately, the Line-Of-Sight (LOS) surface deformation was calculated from the iteratively corrected, unwrapped interferograms.

3 RESULTS AND DISCUSSION

Thirty-four LOS surface deformation maps referenced to the ERS acquisition dated 1996 January 11 were produced by converting the measured phase values (in radians) into displacement values (in millimetre). Deformation associated with surface movements in Greater Cairo is assumed to be vertical. Fig. 3(a) shows the average LOS surface velocity calculated from the 34 surface deformation maps spanning 8 yr (1993–2000). The mean surface velocity map has a minimum negative (subsidence) value and a maximum positive (uplift) value of 7 mm yr^{-1}.

Deformation phase histories of three selected points, A, B and C, are shown in Figs 3(b)–(d) to demonstrate the deformation behaviour of the selected PSs during the period of observation (1993–2000). Locations of the selected points are shown in Fig. 3(a). The deformation phase history of point A (Fig. 3b) demonstrates about 56 mm of surface movement between 1993 and 2000. Deformation occurred away from the satellite (subsidence) with an approximate constant rate over time. The deformation phase history of point B (Fig. 3c) shows a non-linear behaviour of deformation during 1993–2000. About 5 mm of LOS surface movement occurred away from the satellite; however, a local surface movement toward the satellite (uplift) occurred during 1995–1997. The deformation phase history of point C demonstrates about 36 mm of non-linear LOS surface movement toward the sensor between 1993 and 2000. It is obvious that the deformation rate was not constant over the period of observation (Fig. 3d).

To demonstrate the progression of land subsidence over time in Greater Cairo, a time series was created of 34 LOS surface deformation maps interpolated spatially from the originally selected PSs and referenced temporally to the earliest ERS acquisition dated 19963 April 12. Then, eight snapshots (Fig. 4) with 1-yr sampling time interval were taken, and the deformation magnitude and spatial extent were referenced temporally to 1993 July 1. Unfortunately, there

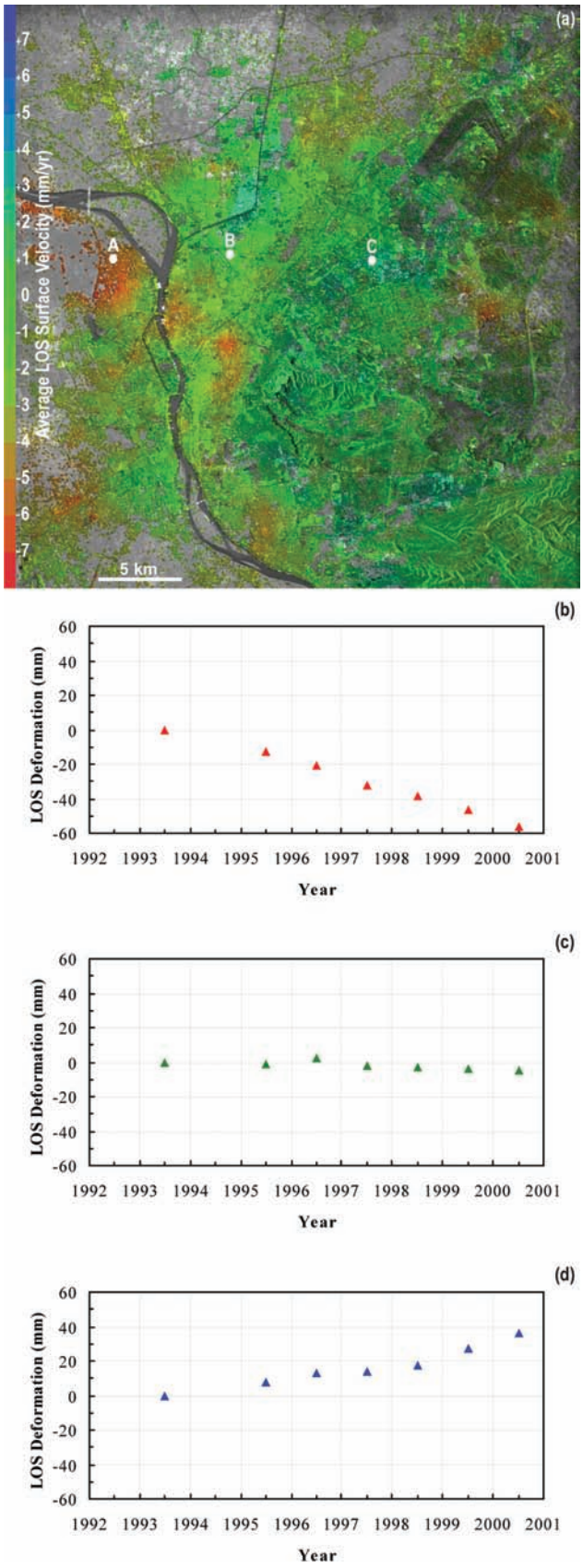

Figure 3. (a) Mean LOS surface velocity between 1993 and 2000, superimposed on the average amplitude image. (b)–(d) Deformation phase histories of points A, B and C, respectively. Locations of the three points are marked with small white dots in (a).

were no ERS acquisitions for the study area during 1994; therefore, we did not create a record for 1994.

The subsidence signals shown in Figs 4(a)–(g) coincide mainly with highly urbanized areas. The highest subsidence rates are observable over the congested, highly populated districts, such as Imbaba, Al-Monira, Ramsis, Ataba, Tahrir and Maadi (Fig. 2). Despite the fact that historical records and location maps of groundwater pumping stations are not available, the coincidence of the interferometric signals with the densely populated districts and the bowl shapes associated with the deformation features imply pumping-induced subsidence due to the presence of a considerable number of pumping stations across the region. The positive variations, which are not aligned with fault segments, in the surface deformation maps are of limited spatial extent and are most likely related to groundwater level recovery and local rebound of the aquifer system rather than gradual uplift that may be caused by a slow tectonic movement.

Pumping-induced subsidence is either recoverable or permanent based upon whether the effective stresses are less or greater than the pre-consolidation stresses (Sneed *et al.* 2001). Rates of groundwater withdrawal vary seasonally in Greater Cairo; withdrawal rates in the summer are significantly higher than those in the other seasons. The non-linear deformation histories demonstrated in Fig. 3 imply that the pumping-induced subsidence might be at least partially recoverable in Greater Cairo. However, the petrophysical and hydrological properties of the aquifer system still have to be addressed. Further analysis has to be undertaken to study the nature and magnitude of seasonal subsidence in Greater Cairo. More frequent InSAR data acquired over a relatively longer time period are still needed to address the impact of pumping-induced subsidence on the long-term subsidence and to determine whether the pumping-induced subsidence is permanent or recoverable in the region.

Tectonic activity in the region has influenced the measured rates of subsidence, as differential surface movements have occurred along the major normal faults. Differential subsidence is observed along the major subsurface fault, 1, trending NE–SW (Fig. 5). The average rate of differential subsidence along the fault is approximately 4 mm yr^{-1}. Differential subsidence also occurred along several surface faults, including faults 2, 3, 4, 5 and 6, with average rates of 3, 4, 3, 3 and 5 mm yr^{-1}, respectively. Subsidence occurred on both sides of the historic surface faults 7 and 8 and the subsurface fault 9.

Previous studies, such as Badawy & Monus (1995), Badawy & Abdel-Fattah (2002) and Korrat *et al.* (2005), showed that north Egypt, especially the area to the south of Cairo, is tectonically active. During the past 15 yr, several major earthquakes have occurred in northern Egypt, for example, 1992 October 12, 1993 July 30, 1993 August 3, 1995 November 22, 1999 October 11, 1999 December 28 and 2001 June 12 (Badawy & Abdel-Fattah 2001). Seismic activities in Greater Cairo along with the ongoing ground subsidence may cause a disaster in the future by activating inactive faults.

The subway network was constructed in 1982 under Cairo. The LOS surface deformation maps suggests that the subway network could be a potential contributing factor to the measured rate of subsidence. The location, extent and magnitude of land subsidence match with several subway stations in Greater Cairo (Fig. 5). The subway network consists of three major lines and approximately 86 stations. The subway lines pass under the most important residential and business districts in Cairo. About six million passengers per day use the subway network (Egyptian Tunneling Society 2005).

The excavation and construction of tunnels, as well as the heavy load of hundreds of trains and millions of passengers every day are potential causes of slight subsidence on the long run, particularly

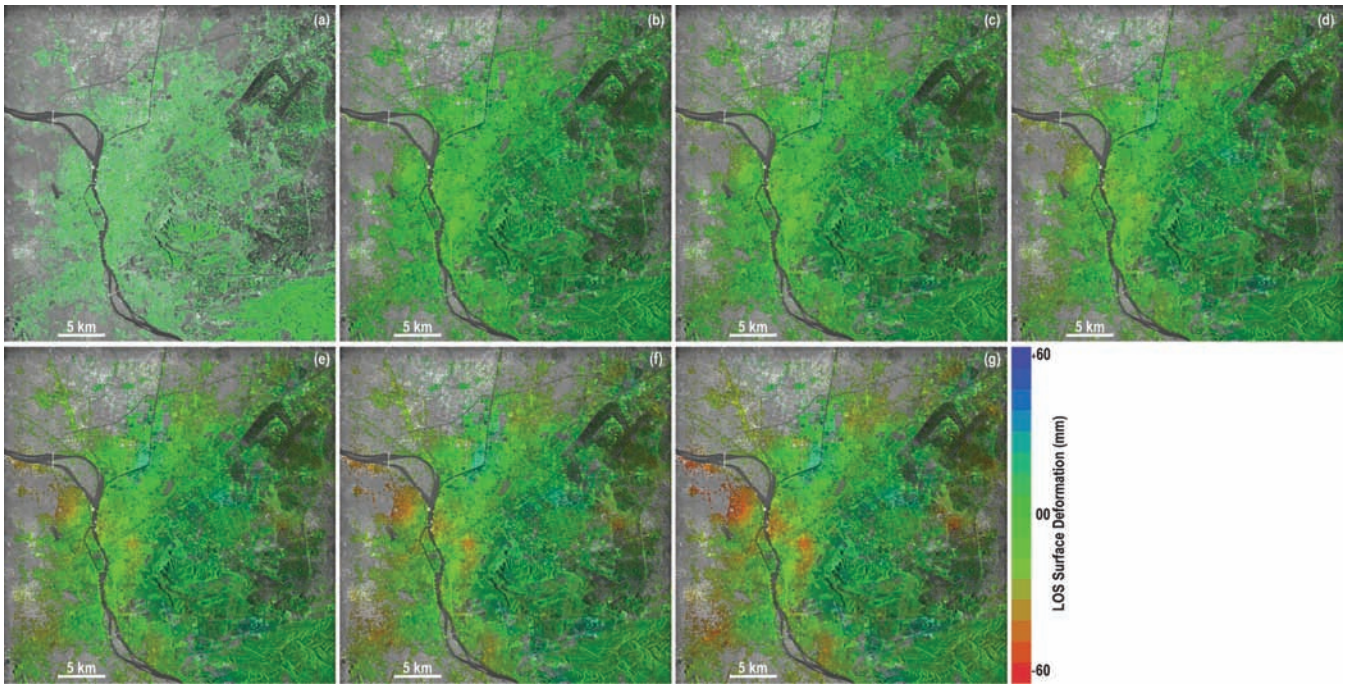

Figure 4. Snapshots of the estimated LOS surface deformation with 1 yr sampling-time interval from 1993 to 2000, superimposed on the average amplitude image: (a) 1993 July 1, (b) 1995 July 1, (c) 1996 July 1, (d) 1997 July 1, (e) 1998 July 1, (f) 1999 July 1 and (g) 2000 July 1.

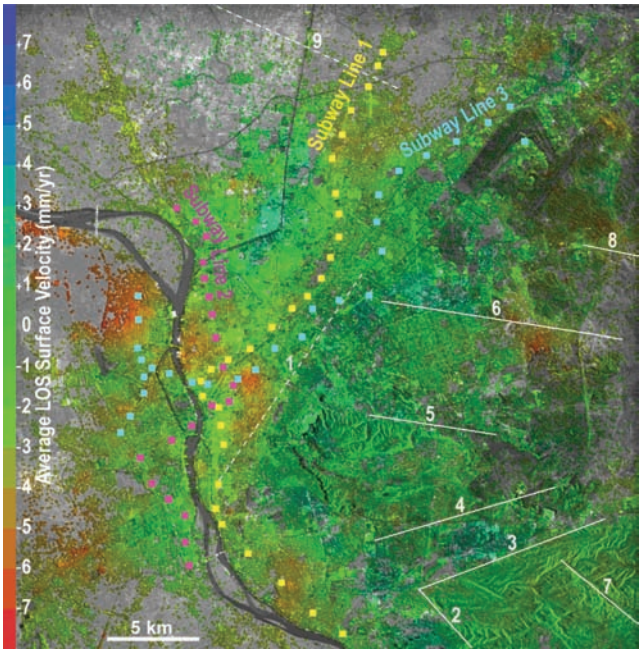

Figure 5. Mean LOS surface velocity during 1993–2000, superimposed on the average amplitude image with major faults (solid white lines are surface faults, dotted white lines are subsurface faults) and subway stations (small square dots). Locations of the major faults are from El Araby & Sultan (2000); unfortunately, we have been unable to find a better fault map.

because the stratigraphic sequence underneath Greater Cairo consists mainly of unconsolidated clays, silts and sands. It is noteworthy that areas where large subway stations are located, such as Ramsis, Ataba and Tahrir, experienced the highest rates of subsidence during 1993–2000. Those areas are characterized also by high population densities. It is also noteworthy that a long section of the subway network (lines 1 and 3) is situated in the subsiding side of fault 1. This situation might be one of the potential causes of subsidence in this area. The subway line 1 started in 1989 and since then it has been always overloaded, more trains are being used and carrying more people than they were designed for. The extra weight of people and trains might be partially responsible for the observed pattern of deformation.

It is not the objective of this study to remediate land subsidence problems in Greater Cairo. However, we propose that the contribution of anthropogenic factors, including the subway network and the withdrawal of groundwater, be re-assessed and differentiated from the impact of natural factors on subsidence. In contrast with the natural factors, such as natural sediment compaction and tectonic activity, which are uncontrollable, the anthropogenic factors can be mitigated. For instance, the overload on subway stations can be reduced in areas of high subsidence rates. Also, the effect of groundwater pumping can be mitigated by discontinuing pumping in sensitive areas. Another approach would be to compensate withdrawal of groundwater by injecting water into the aquifer system. The numerous irrigation channels across the region are a candidate source for the water; however, this approach needs further considerations of the water budget and pollutants in the water.

4 CONCLUSIONS

The slow rate of land subsidence in Greater Cairo in addition to the high level of water vapour content, seasonal cultivation, crop growth and flood irrigation pose a considerable challenge to obtain reliable measurements of subsidence using conventional InSAR techniques. Furthermore, all interferograms created for any time of the year were found impacted by tropospheric variations. However, interferograms created from winter acquisitions were found less impacted by atmospheric artefacts than those created from summer acquisitions.

As the interferometric phase remains well correlated over urban areas for long-time periods, the PS interferometric approach

has been applied in this study to overcome the limitations of conventional InSAR, and to precisely detect and measure land subsidence and its patterns in Greater Cairo during 1993–2000. Results from the PS analysis show the patterns and magnitudes, as well as the non-linear behaviour of land subsidence during 1993–2000. The average measured rate of land subsidence is approximately 7 mm yr^{-1}.

The main contributing factors to the rate of land subsidence in Greater Cairo include natural sediment compaction, groundwater pumping and tectonic activity. Also, the subway network might have a slight impact on the measured rate of subsidence. Differential deformation is detected in several locations along major normal faults in the study area. Pumping-induced subsidence, in urban districts characterized by high population densities, is inferred from the bowl shapes that appear in the surface deformation maps.

Finally, the measured rate of land subsidence in Greater Cairo indicates a pressing need for a regular monitoring regime. The surface deformation maps reveal that the measured rate of subsidence in Greater Cairo is impacted significantly by anthropogenic factors, such as groundwater pumping and the subway network. Therefore, the rate of land subsidence in Greater Cairo can be mitigated by controlling the anthropogenic factors.

ACKNOWLEDGMENTS

This work was supported by the Government of Egypt and the National Aeronautics and Space Administration (NASA), grant NGT5. The ERS images were provided by the European Space Agency (ESA) under a Category-1 Proposal #2774, the SRTM DEM was provided by the Jet Propulsion Laboratory (JPL) and the precise ERS orbital data were provided by the Delft Institute for Earth-Oriented Space Research (DEOS), Delft University of Technology. The authors would like to thank Dr John Beavan, Dr Mahdi Motagh and an anonymous reviewer for their constructive comments and suggestions.

REFERENCES

Adam, N., Kampes, B., Eineder, M., Worawattanamateekul, J. & Kircher, M., 2003. The development of a scientific Permanent Scatterer system, in *High Resolution Mapping from Space, ISPRS/EARSeL Workshop Proceedings,* Hanover, Germany, October 6–8, available at: http://www.ipi.uni-hannover.de/html/publikationen/2003/ workshop/adam.pdf.

Amelung, F., Galloway, D., Bell, J., Zebker, H. & Laczniak, R., 1999. Sensing the ups and downs of Las Vegas: InSAR reveals structural control of land subsidence and aquifer system deformation, *Geology,* **27**(6), 483–486.

Badawy, A. & Abdel-Fattah, A., 2001. Source parameters and fault plane determinations of the 28 December 1999 northeastern Cairo earthquakes, *Tectonophysics,* **343**(1–2), 63–77.

Badawy, A. & Abdel-Fattah, A., 2002. Analysis of the southeast Beni-Suef, northern Egypt earthquake sequence, *J. Geodyn.,* **33,** 219–234.

Badawy, A. & Monus, P., 1995. Dynamic source parameters of the 12th October 1992 Earthquake, Cairo, Egypt, *J. Geodyn.,* **20,** 99–109.

Bawden, G., Thatcher, W., Stein, R., Hudnut, K. & Peltzer, G., 2001. Tectonic contraction across Los Angeles after removal of groundwater pumping effects, *Nature,* **412,** 812–815.

Bell, J.W., Amelung, F., Ferretti, A., Bianchi, M. & Novali, F., 2008, Permanent Scatterer InSAR reveals seasonal and long-term aquifer-system response to groundwater pumping and artificial recharge, *Water Resour. Res.,* **44,** 1–18, W02407, doi:10.1029/2007WR006152.

Buckley, S., Rosen, P., Hensley, S. & Tapley, B., 2003. Land subsidence in Houston, Texas measured by radar interferometry and constrained by extensometers, *J. Geophys. Res.,* **108**(B11), 2542, doi:10.1029/2002JB001848.

Casu, F., Buckley, S., Manzo, M., Pepe, A. & Lanari, R., 2005. Large scale InSAR deformation time series: Phoenix and Houston case studies, in *Geosci. and Remote Sensing Symposium 2005, Vol. 7,* pp. 5240–5243. IEEE, Washington.

Colesanti, C., Ferretti, A., Prati, C. & Rocca, F., 2003. Monitoring landslides and tectonic motions with the Permanent Scatterers technique, *Eng. Geol.,* **68,** 3–14.

Colesanti, C., Le Mouelic, S., Bennani, M., Raucoules, D., Carnec, C. & Ferretti, A., 2005. Detection of mining related ground instabilities using the Permanent Scatterers technique—a case study in the east of France, *Int. Remote Sens.,* **26**(1), 201–207.

Costantini, M., 1998. A novel phase unwrapping method based on network programming, *IEEE Trans. Geosci. Remote Sens.,* **36**(3), 813–821.

Crosetto, M., Arnaud, A., Duro, J., Biescas, E. & Agudo, M., 2003. Deformation monitoring using remotely sensed radar interferometric data, in *Proceedings of the 11th FIG Symposium on Deformation Measurements,* Santorini, Greece, 2003.

Dehls, J., Basilio, M. & Colesanti, C., 2002. Ground deformation monitoring in the Ranafjord area of Norway by means of the permanent scatterer technique, in *Geosci. and Remote Sensing Symposium, 2002, Vol. 1,* pp. 203–207. IEEE, Washington.

Delacourt, C., Briole, P. & Achache, J., 1998. Tropospheric corrections of SAR interferograms with strong topography, Application to Etna, *Geophys. Res. Lett.,* **25,** 2849–2852.

Dixon, T. *et al*., 2006. New Orleans subsidence: space geodesy and Hurricane Katrina Flooding, *Nature,* **441,** 587–588.

Egyptian Tunneling Society (ETS), 2005. Greater Cairo metro network, available at: http://www.egypts.com/index.htm.

El Araby, H. & Sultan, M., 2000. Integrated seismic risk map of Egypt, *Seismol. Res. Lett.,* **71,** 52–65.

Ferretti, A., Prati, C. & Rocca, F., 2000. Nonlinear subsidence rate estimation using Permanent Scatterers in differential SAR interferometry, *IEEE Trans. Geosci. Remote Sens.,* **38**(5), 2202–2212.

Fielding, E., Bloom, R. & Goldstein, R., 1998. Rapid subsidence over oil fields measured by SAR interferometry, *Geophys. Res. Lett.,* **27,** 3215–3218.

Fruneau, B., Rudent, J., Obert, D. & Raymond, D., 1999. Small displacements detected by SAR interferometry on the City of Paris (France), in *Proceedings of the IGARSS′99,* Hamburg, Germany, June 28–July 2 (CD ROM).

Galloway, D. & Hoffmann, J., 2006. The application of satellite differential SAR interferometry-derived ground displacements in hydrogeology, *Hydrogeol. J.,* **15**(1), 133–154, doi:10.1007/s10040–006-0121–5.

Galloway, D., Hudnut, K., Ingebritsen, S., Phillips, S., Peltzer, G., Rogez, F. & Rosen, P., 1998. Detection of aquifer system compaction and land subsidence using interferometric synthetic aperture radar, Antelope Valley, Mojave Desert, California, *Water Resour. Res.,* **34,** 2573–2585.

Goldstein, R. & Werner, C., 1998. Radar interferogram filtering for geophysical applications, *Geophys. Res. Lett.,* **25**(21), 4035–4038.

Hoffmann, J., Zebker, H., Galloway, D. & Amelung, F., 2001. Seasonal subsidence and rebound in Las Vegas Valley, Nevada, observed by synthetic aperture radar interferometry, *Water Resour. Res.,* **37**(6), 1551–1566.

Hooper, A., Zebker, H., Segall, P. & Kampes, B., 2004. A new method for measuring deformation on Volcanoes and other natural terrains using InSAR Persistent Scatterers, *Geophys. Res. Lett.,* **31,** L23611, doi:10.1029/2004GL021737.

Korrat, I., El Agami, N., Hussein, H. & El-Gabry, M., 2005. Seismotectonics of the passive continental margin of Egypt, *J. Afric. Earth Sci.,* **41**(1–2), 145–150.

Massonnet, D. & Feigl, K., 1995. Discrimination of geophysical phenomena in satellite radar interferograms, *Geophys. Res. Lett.,* **22,** 1537–1540.

Motagh, M., Hoffmann, J., Kampes, B., Baes, M. & Zschau, J., 2007. Strain accumulation across the Gazikoy–Saros segment of the North Anatolian Fault inferred from Persistent Scatterer Interferometry and GPS measurements, *Earth planet. Sci. Lett.,* **255**(3–4), 432–444, doi:10.1016/j.epsl.2007.01.003.

Motagh, M., Walter, T.R., Sharifi, M.A., Fielding, E., Schenk, A., Anderssohn, J. & Zschau, J., 2008. Land subsidence in Iran caused by widespread water reservoir overexploitation, *Geophys. Res. Lett.*, **35,** L16403, doi:10.1029/2008GL033814.

Said, R., 1981. *The River Nile*. Springer-Verlag, Berlin, 151 p.

Scharroo, R. & Visser, P., 1998. Precise orbit determination and gravity field improvement for the ERS satellites, *J. geophys. Res.*, **103**(C4), 8113–8127.

Sneed, M., Ikehara, M., Galloway, D. & Amelung, F., 2001. Detection and measuring of land subsidence using Global Positioning System and interferometric synthetic aperture radar, Coachella Valley, California, 1996–1998, U.S. Geological Survey, *Water-Resources Investigations Report*, 01–4193.

Stabel, E. & Fischer, P., 2001. Satellite radar interferometry products for the urban application domain, *Adv. Environ. Res.*, **5,** 425–433.

Stanley, D., 1988. Subsidence in the northeastern Nile Delta: rapid rates, possible causes, and consequences, *Science*, **240,** 497–500.

Stanley, D., 1990. Recent subsidence and northeast tilting of the Nile delta, Egypt, *Mar. Geol.*, **94,** 147–154.

Stanley, D. & Warne, A., 1993. Nile Delta, recent geological evolution and human impact, *Science*, **260,** 628–634.

Strozzi, T. & Wegmüler, U., 1999. Land subsidence in Mexico City mapped by ERS differential SAR interferometry, in *Proceedings of the IGARSS ′99*, Hamburg, Germany, June 28–July 2, pp. 1940–1942.

Strozzi, T., Tosi, L., Carbognin, L., Wegmüler, U. & Galgaro, A., 1999a. Monitoring land subsidence in the Euganean Geothermal Basin with differential SAR interferometry, in *Proceedings of the FRINGE ′99*, Liège, Belgium, 10–12 November, available at: http://earth.esa.int/services/esa_doc/doc_int.html.

Strozzi, T., Wegmüler, U., Luckman, A. & Balzter, H., 1999b. Mapping deformation in Amazon with ERS SAR interferometry, in *Proceedings of the FRINGE ′99*, Liège, Belgium, 10–12 November, available at: http://earth.esa.int/services/esa_doc/doc_int.html.

Warne, A. & Stanley, D., 1993. Late quaternary evolution of the Northwest Nile Delta and adjacent coast in the Alexandria region, Egypt, *J. Coastal Res.*, **9**(1), 26–64.

Zaghloul, Z., Taha, A., Hegab, O. & El-Fawal, F., 1977. The Plio-Pleistocene Nile Delta: sub-environments, stratigraphic section and genetic classification, *Ann. Geol. Surv. Egypt*, **9,** 283–291.

Zebker, H., Rosen, P. & Hensley, S., 1997. Atmospheric effects in interferometric synthetic aperture radar surface deformation and topographic maps, *J. geophys. Res.*, **102**(B4), 7547–7563.